ACS OMEGA

http://pubs.acs.org/journal/acsodf

Article

Magnetic Fractions of $PM_{2.5}$, $PM_{2.5-10}$, and PM_{10} from Coal Fly Ash as Environmental Pollutants

Elena V. Fomenko,* Natalia N. Anshits, Leonid A. Solovyov, Yuriy V. Knyazev, Sergey V. Semenov, Oleg A. Bayukov, and Alexander G. Anshits*

Cite This: *ACS Omega* 2021, 6, 20076−20085

Read Online

ACCESS | Metrics & More | Article Recommendations

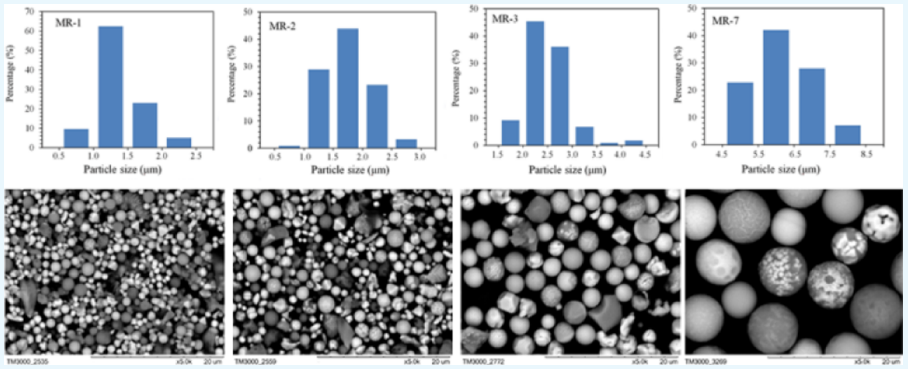

ABSTRACT: Characterization of magnetic particulate matter (PM) in coal fly ashes is critical to assessing the health risks associated with industrial coal combustion and for future applications of fine fractions that will minimize solid waste pollution. In this study, magnetic narrow fractions of fine ferrospheres related to environmentally hazardous $PM_{2.5}$, $PM_{2.5-10}$, and PM_{10} were for the first time separated from fly ash produced during combustion of Ekibastuz coal. It was determined that the average diameter of globules in narrow fractions is 1, 2, 3, and 7 μm. The major components of chemical composition are Fe_2O_3 (57−60) wt %, SiO_2 (25−28 wt %), and Al_2O_3 (10−12 wt %). The phase composition is represented by crystalline phases, including ferrospinel, α-Fe_2O_3, ε-Fe_2O_3, mullite, and quartz, as well as the amorphous glass phase. Mössbauer spectroscopy and magnetic measurements confirmed the formation of nanoscale particles of ε-Fe_2O_3. Stabilization of the ε-Fe_2O_3 metastable phase, with quite ideal distribution of iron cations, occurs in the glass matrix due to the rapid cooling of fine globules during their formation from mineral components of coal.

INTRODUCTION

Coal fly ashes (CFAs) formed during pulverized coal combustion make 60−95%[1,2] of the total amount of solid waste in heat power industry and are industrial byproducts and environmental pollutants. CFAs are multicomponent systems characterized by variable granulometric, chemical, and phase composition. For this very reason, the scope of their application without preliminary classification is limited.[2−5] Worldwide, the key application areas of CFAs involve production of construction materials (concrete, concrete products and grout, cement raw materials, and blended cement) (∼56%); structural fills and road embankments (∼21%); waste stabilization and solidification (∼6%); and application in mining (∼5%) and general engineering (∼4%).[2−7] The annual rates of CFA utilization (Japan, 96%; USA, 65%; China, 45%; EU, 42%; India, 38%; and Russia, 18%) are still low compared to the generated volume, and global consumption of CFAs constitutes only one-fourth of its total production.[5,8]

Separation of individual components [ferrospheres (FSs), cenospheres, and coal char particles][2−5,9−12] has a significant potential to increase the utilization level of CFAs as it allows one to convert industrial waste into industrial raw materials for high-tech applications. The optimal technological option is to separate microspherical components of CFAs in the form of narrow fractions having a certain size, composition, structure, and predictable properties using economically justified and environmentally friendly methods.[13−16] In particular, narrow FS fractions with size ranging from 50 to 250 μm containing 30−92 wt % Fe_2O_3 and exhibiting reproducible magnetic properties have been recovered from different types of CFAs

Received: June 18, 2021
Accepted: July 14, 2021
Published: July 21, 2021

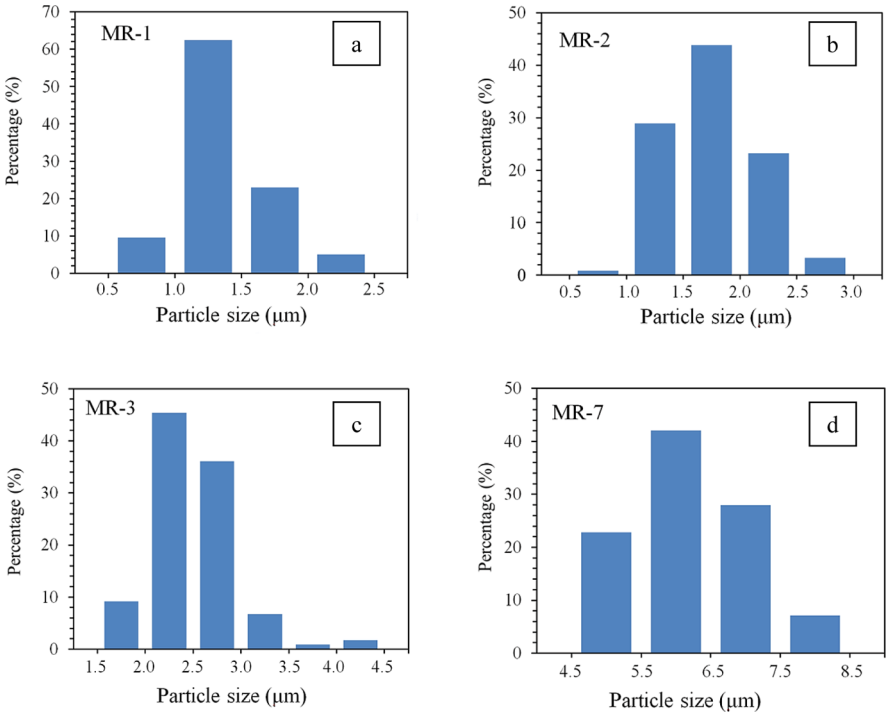

Figure 1. Particle size distribution of magnetic fractions MR-1 (a), MR-2 (b), MR-3 (c), and MR-7 (d).

(S, FS, CS, and FCS) by granulometric, hydrodynamic, and magnetic separation.[17−19] The relationship between the composition, morphology, and microstructure of iron-containing phases has been identified,[14,17] and the key criteria for applicability of narrow fractions of FSs as functional materials have been determined. It has been shown that they can be successfully used to catalyze deep oxidation[20] and oxidative condensation of methane,[21] thermolysis of heavy oil and residual oil,[22] and also can be applied as magnetic carriers for affine core−shell sorbents.[23]

Dispersed particular matter with an aerodynamic diameter <10 μm (PM_{10}) is the environmentally hazardous component of CFAs. Its content ranges from 6 to 40%[24−26] depending on coal type and combustion conditions. Particulate matter (PM) with an aerodynamic diameter between 2.5 and 10 μm ($PM_{2.5-10}$) is classified as "coarse"; less than 2.5 μm ($PM_{2.5}$) is classified as "fine"; and less than 0.1 μm ($PM_{0.1}$) is classified as "ultrafine" particles. All these particles are harmful to human health and can be subdivided into the following groups depending on depth of their penetration into the body: *inhalable particles* (particles that usually do not penetrate deeper than the bronchi), *thoracic particles* (particles that reach terminal bronchioles and are accumulated in the lungs), and *respirable particles* (particles that can enter the bloodstream).[27]

Iron-rich magnetic particles in PM_{10} from CFAs have an increased harmful effect on human health and the ecosystem. They induce apoptosis in human bronchial cells and should be considered an environmental inhalation hazard.[28] Furthermore, these particles are among the anthropogenic sources of magnetic pollution[29] that are currently viewed within the concept of environmental magnetism.[30,31]

In contrast to the coarse fractions of FSs,[17−19] there are almost no available literature data on extraction of their fine fractions with narrow particle size distribution or systematic data on the composition, structure, and properties that would characterize the magnetic particles in $PM_{2.5}$, $PM_{2.5-10}$, and PM_{10} from CFAs. Such factors as spherical shape of dispersed FSs, the simultaneous combination of magnetic properties and high thermal stability, as well as the possibility of performing surface functionalization are crucial for using these particles to successfully design microspherical functional materials (including composite sorbents with the core−shell structure, magnetic carriers, affine sorbents, and biosensors).[23] Detailed investigation of separable CFA components will allow one to use them in new areas and minimize solid waste pollution.

The aim of this study was to perform comprehensive characterization of narrow fractions of fine FSs related to magnetic $PM_{2.5}$, $PM_{2.5-10}$, and PM_{10} produced from fly ash of Ekibastuz coal (one of the high-ash coal consumed in Russia) using scanning electron microscopy (SEM) and energy-dispersive X-ray spectroscopy (EDS), X-ray powder diffraction analysis, Mössbauer spectroscopy, and magnetic techniques. The findings obtained in this study can be used to identify promising applications for hazardous dispersed FSs, are needed to quantify the environmental magnetic pollution affected by coal-fired power plants, and can be used as reference for anthropogenic PM.

RESULTS AND DISCUSSION

The target fractions of FSs related to magnetic $PM_{2.5}$, $PM_{2.5-10}$, and PM_{10} were obtained by aerodynamic classification followed by magnetic separation from fly ash, which was sampled locally from field 1 of an EGA four-field electrostatic precipitator. The physicochemical characteristics of fly ash and the technological scheme for extracting fine narrow fractions from it were reported in ref 32.

Particle Size Distribution and Globule Morphology of Magnetic Fractions. Magnetic fractions of fine FSs isolated from finely dispersed fractions of fly ash[32] are characterized by narrow particle size distribution (Figure 1) and certain average diameter d_{av} (denoted by a number in the sample name): MR-1, MR-2, MR-3, and MR-7. The finest fraction, MR-1, contains

https://doi.org/10.1021/acsomega.1c03187
ACS Omega 2021, 6, 20076−20085

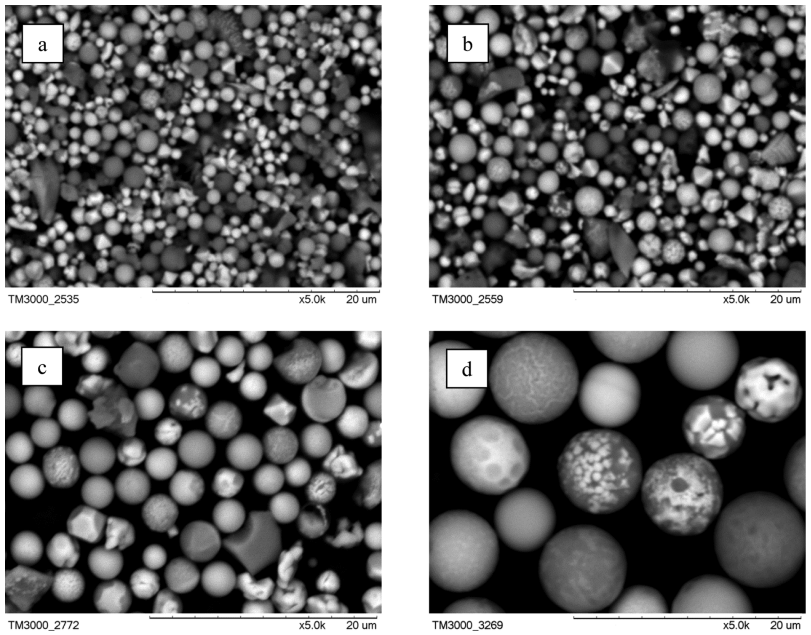

Figure 2. SEM images of magnetic fractions MR-1 (a), MR-2 (b), MR-3 (c), and MR-7 (d).

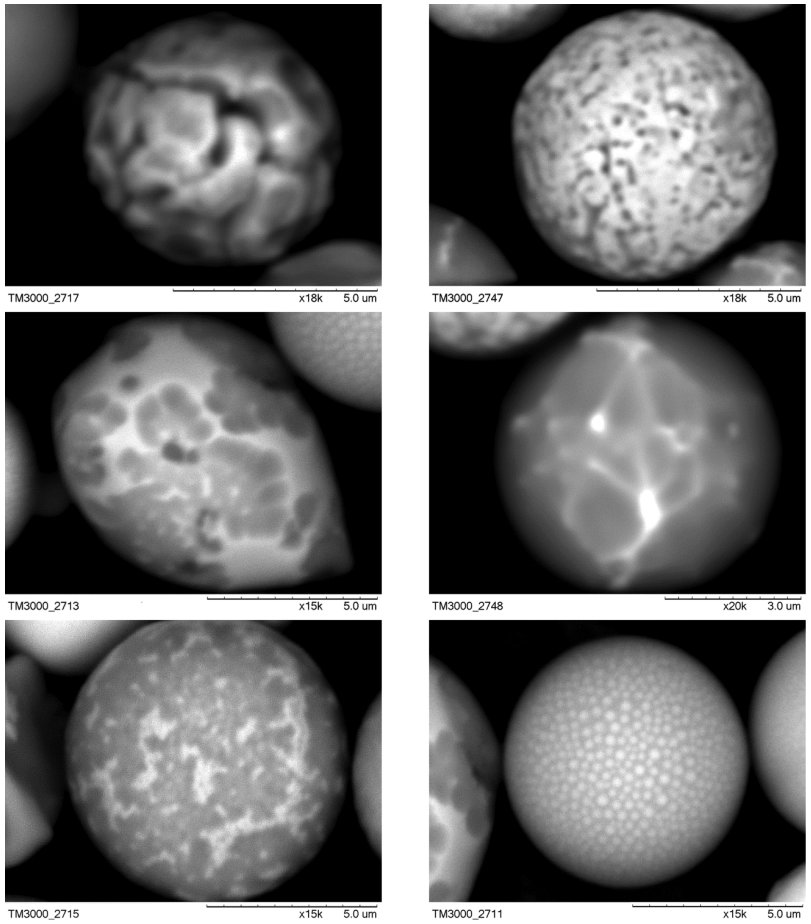

Figure 3. SEM images of individual FSs in the magnetic fraction MR-7.

particles sized <2.5 μm (10%, <1 μm) and refers to "fine" $PM_{2.5}$. The MR-2 fraction contains 97% of the $PM_{2.5}$ particle; more than half of all particles in the MR-3 fraction (~55%) are sized <2.5 μm. The coarsest fraction, MR-7, is represented by particles with a diameter ranging between 4.5 and 8.5 μm and is classified as "coarse" $PM_{2.5-10}$.

The survey SEM images of the magnetic fraction show that most particles typically have a spherical shape (Figure 2). The morphological types of fine FSs have been singled out for

https://doi.org/10.1021/acsomega.1c03187
ACS Omega 2021, 6, 20076−20085

individual globules of the MR-7 fraction (Figure 3). As an example, blocklike spherical particles, previously identified in large fractions,[34,35] are shown in Figure 4 for MR-2 fraction.

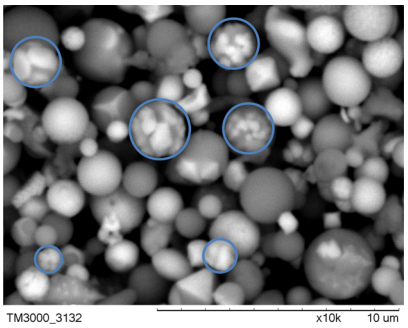

Figure 4. SEM image of magnetic fractions MR-2 with the designation of blocklike FSs.

Chemical and Phase Composition of Magnetic Fractions. In terms of their chemical composition (Table 1), the dispersed fractions of FSs belong to the Fe_2O_3−SiO_2−Al_2O_3 system; the total amount of the major components in this system is as high as 95−96 wt % (including 57−60 wt % Fe_2O_3, 25−28 SiO_2, and 10−12 wt % Al_2O_3). X-ray diffraction (XRD) analysis (Table 1) has revealed that narrow fractions of FSs contain crystalline iron-bearing phases, including ferrospinel, α-Fe_2O_3 and ε-Fe_2O_3, mullite and quartz phases, and the amorphous glass phase. Quantifying the contents of iron-rich phases in fine fractions of FSs is an important part in understanding the health risks associated with magnetic pollution from CFAs.[36−38] Unfortunately, little information is still available about the actual phase composition of anthropogenic magnetic particles, although the concentration of Fe in PM is often determined.[36,39]

Table 1. Chemical and Phase Composition (wt %) of Magnetic Fractions[a]

	MR-1	MR-2	MR-3	MR-7
SiO_2	26.5	27.8	27.4	25.2
Al_2O_3	12.4	11.3	9.8	10.0
Fe_2O_3	57.1	57.0	58.9	60.1
CaO	1.4	1.5	1.7	2.3
MgO	2.0	1.8	1.8	1.9
Na_2O	0.5	0.4	0.3	0.4
K_2O	0.3	0.3	0.2	0.2
glass phase	n/d	n/d	38.9	44.5
mullite	6.0	6.0	2.5	1.4
quartz	5.0	6.0	2.3	1.4
Fe-spinel	66.0	64.0	39.9	39.9
α-Fe_2O_3	2.0	2.0	2.5	3.6
ε-Fe_2O_3	21.0	22.0	13.9	9.2

[a]n/d—the content of the glass phase was not determined; the quantitative phase composition was determined only for the crystalline component.

The dependences between the contents of individual components of the narrow fractions of FSs and particle size have been identified. The contents of Fe_2O_3 and CaO increase as the d_{av} parameter rises from 1 to 7 μm. Changes in the phase composition depending on particle size can be adequately assessed by performing quantitative analysis of the MR-3 and MR-7 fractions, including measuring the content of the glass phase (Table 1). Thus, the glass-phase content rises as d_{av} increases from 3 to 7 μm, while the concentrations of the mullite and quartz phases decrease. For the iron-containing phases, α-Fe_2O_3 concentration increases and ε-Fe_2O_3 content decreases, while the concentration of the ferrospinel phase remains unchanged (Table 1). It is fair to assume that stabilization of the metastable ε-Fe_2O_3 phase in the glass matrix of FSs occurs due to the rapid cooling of fine globules during their formation from the mineral precursors initially contained in coal.

Mössbauer Spectroscopy. The Mössbauer spectra of the narrow fractions of dispersed FSs are shown in Figure 5. The spectral lines form Zeeman sextet patterns, whose appearance indicates that there are several components. In accordance with the XRD data, the main X-ray detectable phases in the samples are as follows: spinel, the ε- and α-polymorphic forms of iron(III) oxide, and to a lesser extent, quartz and mullite (which corresponded to the quadrupole doublet signals).

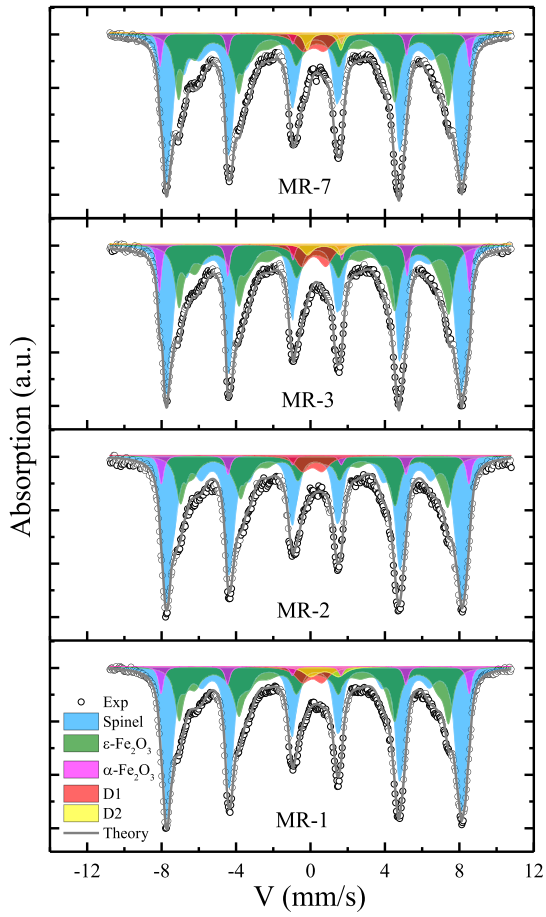

Figure 5. Mössbauer spectra of magnetic fractions. The dots show the experimental spectra, the filled areas correspond to the sum of the subspectra of the detected crystallographic phases, and the solid line is the processing result.

Table 2 summarizes the results of identification of the spectra. These parameters allow one to identify the iron-containing phases. The last column in Table 2 shows the total content of the crystalline phases detected in the narrow fractions of FSs according to the Mössbauer spectroscopy data. These findings are consistent with the XRD data (Table 1).

https://doi.org/10.1021/acsomega.1c03187
ACS Omega 2021, 6, 20076−20085

Table 2. Mössbauer Parameters of Magnetic Fractions[a]

	IS, ±0.005 mm/s	H_{hf}, ±10 kOe	QS, ±0.02mm/s	W, ±0.02 mm/s	A, ±0.03 au	position/phase	phase content, au
				MR-1			
S1	0.407	515	−0.17	0.31	0.05	α-Fe_2O_3	0.05
S2	0.446	497	0.00	0.36	0.13	A-substituted $Fe3O_4$	0.59
S3	0.682	453	0.00	0.55	0.04	B-substituted $Fe3O_4$	
S4	0.261	496	0	0.38	0.17	γ-Fe2O3	
S5	0.339	476	0.00	0.48	0.12	substituted γ-Fe_2O_3	
S6	0.389	380	0	0.30	0.12	B-spinel	
S7	0.382	450	−0.34	0.55	0.16	Fe1 + Fe2 ε-Fe_2O_3	0.31
S8	0.504	406	−0.28	0.82	0.08	Fe3 ε-Fe_2O_3	
S9	0.315	266	0	1.11	0.07	Fe4 ε-Fe_2O_3	
D1	0.206		1.06	0.93	0.04	paramagnetic	
D2	0.877		1.51	0.96	0.03	paramagnetic	
				MR-2			
S1	0.414	514	−0.20	0.32	0.05	α-Fe_2O_3	0.05
S2	0.454	495	0.00	0.39	0.14	A-substituted Fe_3O_4	0.61
S3	0.744	454	0	0.25	0.02	B-substituted Fe_3O_4	
S4	0.265	494	0	0.40	0.19	γ-Fe_2O_3	
S5	0.357	470	0.00	0.56	0.14	substituted γ-Fe_2O_3	
S6	0.404	383	0	0.30	0.14	B-spinel	
S7	0.426	447	−0.43	0.51	0.14	Fe1 + Fe2 ε-Fe_2O_3	0.27
S8	0.564	413	−0.53	0.81	0.07	Fe3 ε-Fe_2O_3	
S9	0.238	261	0	0.89	0.06	Fe4 ε-Fe_2O_3	
D1	0.252		0.73	1.95	0.05	paramagnetic	
				MR-3			
S1	0.406	517	−0.32	0.26	0.06	α-Fe_2O_3	0.06
S2	0.456	497	−0.03	0.31	0.11	A-substituted Fe_3O_4	0.50
S3	0.776	454	0	0.51	0.05	B-substituted Fe_3O_4	
S4	0.259	496	0	0.33	0.14	γ-Fe_2O_3	
S5	0.336	476	0	0.47	0.13	substituted γ-Fe_2O_3	
S6	0.403	377	0.03	0.19	0.08	B-spinel	
S7	0.391	451	−0.34	0.53	0.16	Fe1 + Fe2 ε-Fe_2O_3	0.34
S8	0.546	408	−0.17	0.92	0.11	Fe3 ε-Fe_2O_3	
S9	0.297	261	0	1.04	0.08	Fe4 ε-Fe_2O_3	
D1	0.142		1.30	0.88	0.05	paramagnetic	
D2	0.839		1.73	0.64	0.04	paramagnetic	
				MR-7			
S1	0.405	516	−0.26	0.28	0.05	α-Fe_2O_3	0.05
S2	0.450	497	−0.03	0.35	0.12	A-substituted Fe_3O_4	0.55
S3	0.706	458	0	0.46	0.06	B-substituted Fe_3O_4	
S4	0.262	495	0	0.35	0.14	γ-Fe_2O_3	
S5	0.318	475	0.00	0.45	0.11	substituted γ-Fe_2O_3	
S6	0.375	387	0	0.21	0.13	B-spinel	
S7	0.375	451	−0.35	0.53	0.17	Fe1 + Fe2 ε-Fe_2O_3	0.33
S8	0.615	408	−0.43	0.81	0.08	Fe3 ε-Fe_2O_3	
S9	0.285	265	0	1.21	0.08	Fe4 ε-Fe_2O_3	
D1	0.116		1.10	1.03	0.04	paramagnetic	
D2	0.786		1.80	0.40	0.02	paramagnetic	

[a]IS—isomer chemical shift from αFe, H_{hf}—hyperfine field, QS—quadruple splitting, W is the half-line width, and A is the area of the corresponding component (the iron occupation factor).

The Mössbauer spectroscopy allowed us to identify the iron-containing phases within the narrow fractions of FSs. According to our data, the spinel with different degrees of iron cation substitution (50−61 at. %) is the main phase. In all the samples, the phase of the substituted magnetite (Table 2, substituted Fe_3O_4) is characterized by a very low content of iron cations occupying octahedral sites (the $Fe^{2.5+}$ state).[40,41] It is fair to assume that the spinel phase is mainly contained in magnetite, with the preferential dilution of iron cations at octahedral sites.[42] Furthermore, the Mössbauer spectroscopy data demonstrate that the narrow fractions of FSs contain a highly substituted spinel phase (Table 2, B-spinel), which is characterized by a weak hyperfine field (~380 kOe) due to the high degree of substitution. It should also be mentioned that the samples contain maghemite γ-Fe_2O_3; this phase actually refers to magnetite with non-occupied cationic sites (vacancies), which can reside both at the tetrahedral and octahedral positions.[42]

Along with the spinel phase, a rare modification of iron oxide ε-Fe_2O_3 has been identified in the narrow fractions of FSs.[43−45]

https://doi.org/10.1021/acsomega.1c03187
ACS Omega 2021, 6, 20076−20085

It is known that the ε-Fe_2O_3 modification is metastable and can exist only in the nano-sized form and within a very narrow size range (2−30 nm).[45,46] If particle size increases, the crystal structure changes, and transition into the thermodynamically stable phase of hematite α-Fe_2O_3 takes place. In our earlier study, we reported that the polymorphic species ε-Fe_2O_3 (at concentrations of 0.3−2.8 wt %) is formed in coarse fractions of FSs recovered from fly ashes produced during combustion of Ekibastuz coal.[14] Sutto (ref 38) reported that the purified magnetic component with a particle size of 10−20 μm recovered from coal ash at Kentucky power plant contains 8.7% ε-Fe_2O_3. It is clear that the ε-Fe_2O_3 content is closely related to the size of globules being formed. Since micron-sized particles are cooled down quicker, it limits the growth of iron oxide nanoparticles, resulting in stabilization of ε-Fe_2O_3 at high concentrations.

Another feature of the polymorphic form ε-Fe_2O_3 is that it cannot exist independently and its particles can reside in the silicon oxide matrix.[45,47] Particles localized in the SiO_2 matrix are poorly discernible by XRD analysis and can be identified as a component of the glass phase. It is important to mention that iron distribution over the four non-equivalent positions of ε-Fe_2O_3 in FSs is close to the ideal ordered state of the phase for which the (Fe1 + Fe2 + Fe3)/Fe4 ratio is equal to 3.[48]

The Mössbauer parameters of the detected crystalline phases and their contents in FSs are virtually the same for all narrow fractions, which may indicate that the entire silicate glass crystal matrix has a similar chemical composition. The contents of hematite and paramagnetic iron species, which may correspond to the glass phase and mullite,[49] can also be considered constant.

Magnetization Measurements. Figure 6 shows the results of magnetic measurements of the narrow fractions of

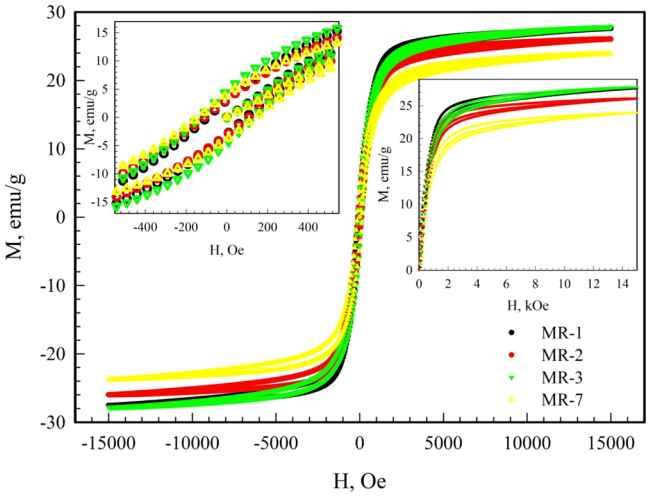

Figure 6. Field dependence of magnetization for magnetic fractions at 300 K. The insets show the enlarged regions of hysteresis (left) and saturation magnetization (right).

dispersed FSs. The experimental magnetic characteristics are listed in Table 3. The resulting dependences of magnetization show the integral contribution from each crystalline phase in the samples. This explains the observed hysteresis loop broadening in the high-field region (see the inset in Figure 6). The coercivity of ε-Fe_2O_3 can be up to 20 kOe; however, this parameter is very sensitive to nanoparticle size.[45,50]

Table 3. Magnetic Characteristics of Magnetic Fractions[a]

fraction	H_c, ±1 Oe	M_{rem}, ±0.05 emu/g	M_{sat}, ±0.05 emu/g	M_{rem}/M_{sat}
MR-1	96	3.0	29.1	0.103
MR-2	111	3.1	27.4	0.113
MR-3	135	4.6	29.3	0.157
MR-7	141	4.0	25.4	0.157

[a]H_c—coercivity, M_{rem}—remanence, and M_{sat}—saturation magnetization.

Meanwhile, magnetite and maghemite have an almost zero coercivity.[51,52]

Since the size of ε-Fe_2O_3 particles is ridiculously small compared to the diameter of FSs and can vary within a very narrow range, their contribution to changes in coercivity can be neglected. If we assume that the shape of microcrystals remains constant, the observed monotonically increasing coercivity (H_c) can be attributed to the increase in the average size of globules. This process is also responsible for growth of microcrystals of the substituted magnetite. The coercivity of magnetite microcrystals can increase only for single-domain particles.[53,54] The critical size of magnetite single-domain particles strongly depends on their shape anisotropy and lies within the range of 40−120 nm for spherical particles.[54,55] Therefore, it can be viewed that single-domain microparticles of substituted magnetite are formed in the selected range of FS size.

Saturation magnetization (M_{sat}) shows the saturation magnetic moment in strong magnetic fields and corresponds to the integral magnetic moment of the entire sample. This parameter is weakly dependent on particle size. Since ε-Fe_2O_3 nanoparticles are very small, magnetite makes the main contribution to M_{sat}. For non-substituted bulk magnetite, the parameter M_{sat} is equal to 90 emu/g.[53,56] For FSs, the decline in this parameter can be attributed to the nanosize of the crystals and significant substitution at the octahedral position, which is consistent with the Mössbauer spectroscopy data.

Johnson et al. (ref 51) studied magnetite samples with particle size <44 μm (the average size being ~2 μm). They showed that the ratio between remanence and saturation magnetization (M_{rem}/M_{sat}) for these samples at room temperature is 8.6%, thus indicating that the sample has a multidomain morphology.[53] However, the M_{rem}/M_{sat} ratio observed in the FS samples is somewhat higher and does not correspond to the single-domain state criterion proposed by Stoner and Wohlfarth.[57] Meanwhile, this parameter depends on the particles' shape, and the long thin single domain rods give a somewhat reduced value of M_{rem}/M_{sat} ~0.40.[51] Magnetic measurements of the samples of biogenic sedimentary magnetites showed that the M_{rem}/M_{sat} ratio for pseudo-single-domain particles lay in the range of 0.1−0.2, being consistent with our results (Table 3).[58] Taking into account the shape anisotropy of the substituted magnetite microparticles, the resulting underestimated M_{rem}/M_{sat} ratios for the narrow fractions of FSs can be attributed to several factors: (1) the appreciably high weight content of the glass phase in the samples; (2) the effect of cationic substitution of iron; and (3) strong anisotropy of particle shape.

CONCLUSIONS

The present study leads to the following conclusions. Magnetic narrow fractions of fine FSs with the average globule diameter of 1, 2, 3, and 7 μm were for the first time separated from fly

https://doi.org/10.1021/acsomega.1c03187
ACS Omega 2021, 6, 20076−20085

ash formed during pulverized combustion of Ekibastuz coal. The chemical composition of narrow fractions related to environmentally hazardous $PM_{2.5}$, $PM_{2.5-10}$, and PM_{10} is mainly represented by Fe_2O_3, SiO_2, and Al_2O_3 (57−60, 25−28, and 10−12 wt %, respectively). The phase composition includes an amorphous glass phase, crystalline iron-containing phases (ferrospinel, α-Fe_2O_3, and ε-Fe_2O_3), as well as the mullite and quartz phases. It was found that the Fe_2O_3 and CaO contents increase as the average diameter of FSs in narrow fractions rises from 1 to 7 μm. As the average diameter of FSs increases from 3 to 7 μm, the content of the glass phase increases, while the contents of mullite and quartz decline. For iron-containing phases, α-Fe_2O_3 concentration is increased and ε-Fe_2O_3 concentration is decreased, while the content of the ferrospinel phase remains constant. Mössbauer spectroscopy and magnetic measurements revealed the nano-sized ε-Fe_2O_3 oxide phase present in fine FSs. Stabilization of the metastable ε-Fe_2O_3 phase in the glass matrix of FSs occurs due to the rapid cooling of fine globules during their formation. Furthermore, the fast cooling process results in a quite ideal distribution of iron cations over four nonequivalent positions in the ε-Fe_2O_3 phase. According to our magnetization measurements, we suppose that the formation of substituted magnetite microcrystals with a single- or pseudo-single domain state takes place. The results of comprehensive characterization of fine magnetic narrow fractions can be used to identify promising applications of hazardous $PM_{2.5}$, $PM_{2.5-10}$, and PM_{10}, including the development of new microspherical functional materials (composite sorbents with the core−shell structure, magnetic carriers, affine sorbents, biosensors, and etc.). In addition, they are needed to quantify magnetic pollution and can be used as reference for anthropogenic PM from coal-fired power plants. Further research will focus on the systematic study of the major component compositions of individual dispersed FSs and particle structure, as well as investigation of the features of FS formation routes and the nature of mineral precursors controlling the FS structure.

EXPERIMENTAL SECTION

Preparation of Magnetic Fractions. As the raw material for the extraction of target fractions of fine FSs, we used fly ash produced by combustion of pulverized hard coal of grade SS (mvb) from the Ekibastuz Basin. Combustion was carried out at the Reftinskaya Power Station (PK-39-2, P-57-2, and P-57-3 boiler unit; flame kernel temperature, 1520−1550 °C; dry ash handling system). Fly ash was sampled locally from field 1 of an EGA four-field electrostatic precipitator. The narrow fractions of FSs related to magnetic $PM_{2.5}$, $PM_{2.5-10}$, and PM_{10} were obtained by aerodynamic separation followed by magnetic separation. Aerodynamic separation was performed on a 50 ATP centrifugal laboratory classifier (Hosokawa ALPINE, Germany). Magnetic separation was performed in distilled water using a neodymium magnet (NdFeB, F—24 lb). The physicochemical characteristics of initial fly ash and the technological scheme for extracting fine narrow fractions from it were reported in ref 32.

Characterization Methods. Narrow fractions of FSs were characterized by the following parameters: particle size distribution, average globule diameter, chemical and phase composition, Mössbauer parameters (isomer chemical shift from αFe, quadrupole splitting, the Mössbauer line width at half-height, hyperfine field, and the relative population), and magnetic characteristics (coercivity, remanence, and saturation magnetization).

Particle size distribution and the average diameter d_{av} of globules were determined from the SEM images of narrow fractions using the Image Tool v.3.0 software package (Uthscsa, USA); 4−8 linear measurements of the individual globule diameter were carried out, and the arithmetic mean was calculated. The value of average diameter for each narrow fraction was denoted by a number in the sample name: MR-1, MR-2, MR-3, and MR-7.

SEM−EDS were used to determine the chemical composition of narrow fractions. The studies were carried out on an TM-3000 scanning electron microscope (Hitachi, Japan) equipped with a Quantax 70 microanalysis system with a Bruker XFlash 430H energy-dispersive X-ray spectrometer. The analysis was carried out according to the procedure reported in ref 33. Powder samples were applied onto a double-coated conductive carbon adhesive tape (Ted Pella Inc., USA) attached to a flat substrate (1−3 mm thick and 30 mm in diameter) fabricated using DuoPUR poly(methyl methacrylate) resin (Adler, Austria). A graphite disk with the powder sample applied onto it was immobilized on the microscope stage using carbon tape; images of three surface regions of the samples were recorded at a magnification of 1000× and an accelerating voltage of 15 kV. The data acquisition time was 10 min, which enabled quantitative processing of the spectra. As an example, Figure 7 shows the

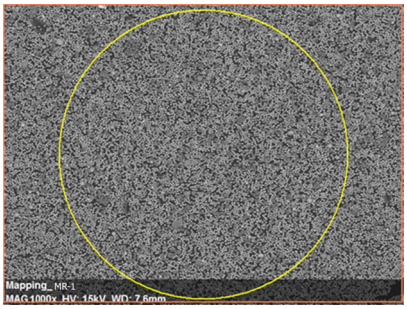

Figure 7. SEM image of magnetic fraction MR-1, indicating the areas of analysis.

SEM image of narrow fraction, indicating the area of analysis. The contents of elements (Si, Al, Fe, Ca, Mg, K, and Na) were determined for each surface region; the elemental compositions were expressed as oxides, and their sum was set to 100%. The arithmetic mean of the oxide content determined for the three surface areas was taken as the final result (Table 1). The standard deviation (σ) did not exceed ±0.3 for SiO_2, ±0.2 for Al_2O_3, ±0.6 for Fe_2O_3, ±0.2 for MgO, ±0.1 for CaO, Na_2O, and K_2O.

X-ray powder diffraction analysis was used to determine the quantitative phase composition of narrow fractions of dispersed FSs. The XRD data (Figure 8) were obtained on an X'Pert Pro MPD powder diffractometer (PANalytical, the Netherlands) with a PIXcel solid-state detector. The contents of the major crystalline phases were determined by Rietveld full-profile analysis with derivative difference minimization according to the procedure used previously for coarse fractions of FSs.[14] The weight content of the X-ray amorphous component was determined by the external standard method with hematite used as the standard. The absorption coefficients of the samples for the Co Kα radiation were calculated from

https://doi.org/10.1021/acsomega.1c03187
ACS Omega 2021, 6, 20076−20085

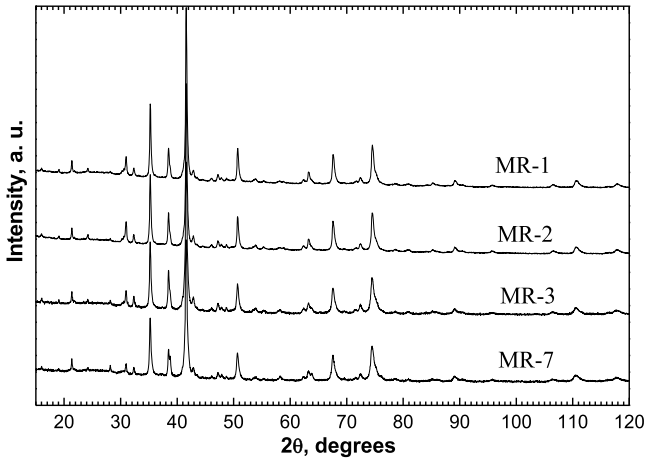

Figure 8. XRD patterns of magnetic fractions.

the total elemental composition according to the chemical analysis data. The contents of crystalline phases and glass-phase are listed in Table 1.

Mössbauer spectra of the narrow fractions of dispersed FSs (Figure 5) were measured using the standard MS1104Em spectrometer in the constant acceleration mode with the 512-channels detector. A mobile source of ^{57}Co(Rh) γ-ray photons was at room temperature. Experimental samples were fixed in a polymer iron-free holder so that the sample was perpendicular to the propagation direction of gamma rays. Interpretation of the spectra was performed in two stages. At the first stage, we determined the probability distribution of quadrupole splitting, P(QS), and hyperfine field, P(H), in the spectrum. Such calculation gives possible nonequivalent iron states in the samples.[59] To perform the P(QS)/P(H) calculation, the experimental spectrum was filled by a number of doublets/sextets with Lorentzian line-form and natural line-width [W = 0.24 mm/s for ^{57}Co(Rh) source] and QS/H_{hf} with the step Δ = 0.01 mm/s (1.3 kOe) [in our case, from 0.00 to 2.2 mm/s (200−560 kOe)]. Then, the isomer shift and intensity of Mössbauer lines were varied. As a result, we obtained the set of the intensities corresponding to each doublet/sextet in our series. These data conform to the probability of each doublet/sextet existence in the experimental spectrum. Then, based on these calculations, we formed a preliminary spectrum. It contained a set of Mössbauer doublets, corresponding to possible nonequivalent positions and modeling as a group of the analytical functions. This group was fitted to the experimental spectrum by varying the entire set of hyperfine parameters using the least-squares method in the linear approximation (χ^2 criterion). Mössbauer absorption lines were represented by the pseudo-Voight function, following the eq 1.

$$I = I\left(\frac{k}{(1 + x_i)^2} + (1 - k)\cdot e^{-\ln 2\cdot x_i^2}\right) \quad (1)$$

here, $x_i = 2\cdot\left(\frac{IS - i}{W}\right)$, i—is a channel number. I, IS, and W are hyperfine parameters (line intensity, isomer shift, and line-width, respectively), k—is the Lorentz−Gauss parameter, which determines the absorption line form. In our case, the approximation of the Lorentz form was used, that is, k = 1. Table 2 summarizes the results of identification of the spectra.

The magnetic measurements (Figure 6) of the narrow fractions of dispersed FSs were performed on a LakeShore VSM 8604 vibrating sample magnetometer at room temperature in a constant magnetic field of 0−15,000 Oe, with an increment of 50 Oe. The experimental magnetic characteristics are listed in Table 3.

AUTHOR INFORMATION

Corresponding Authors

Elena V. Fomenko − *Institute of Chemistry and Chemical Technology SB RAS, Federal Research Center "Krasnoyarsk Science Center SB RAS", Krasnoyarsk 660036, Russia;* orcid.org/0000-0003-0929-807X; Email: fom@icct.ru

Alexander G. Anshits − *Institute of Chemistry and Chemical Technology SB RAS, Federal Research Center "Krasnoyarsk Science Center SB RAS", Krasnoyarsk 660036, Russia; Siberian Federal University, Krasnoyarsk 660041, Russia;* orcid.org/0000-0002-5259-0319; Email: anshits@icct.ru

Authors

Natalia N. Anshits − *Institute of Chemistry and Chemical Technology SB RAS, Federal Research Center "Krasnoyarsk Science Center SB RAS", Krasnoyarsk 660036, Russia*

Leonid A. Solovyov − *Institute of Chemistry and Chemical Technology SB RAS, Federal Research Center "Krasnoyarsk Science Center SB RAS", Krasnoyarsk 660036, Russia*

Yuriy V. Knyazev − *Kirensky Institute of Physics SB RAS, Federal Research Center "Krasnoyarsk Science Center SB RAS", Krasnoyarsk 660036, Russia*

Sergey V. Semenov − *Kirensky Institute of Physics SB RAS, Federal Research Center "Krasnoyarsk Science Center SB RAS", Krasnoyarsk 660036, Russia; Siberian Federal University, Krasnoyarsk 660041, Russia*

Oleg A. Bayukov − *Kirensky Institute of Physics SB RAS, Federal Research Center "Krasnoyarsk Science Center SB RAS", Krasnoyarsk 660036, Russia*

Complete contact information is available at: https://pubs.acs.org/10.1021/acsomega.1c03187

Notes

The authors declare no competing financial interest.

ACKNOWLEDGMENTS

This work was conducted within the framework of the budget project # # 121031500198-3 for Institute of Chemistry and Chemical Technology SB RAS using for SEM−EDS and magnetic studies the equipment of Krasnoyarsk Regional Research Equipment Centre of SB RAS.

REFERENCES

(1) Vassilev, S. V.; Vassileva, C. G. Methods for characterization of composition of fly ashes from coal-fired power stations: A critical overview. *Energy Fuels* **2005**, *19*, 1084−1098.

(2) Yao, Z. T.; Ji, X. S.; Sarker, P. K.; Tang, J. H.; Ge, L. Q.; Xia, M. S.; Xi, Y. Q. A comprehensive review on the applications of coal fly ash. *Earth-Sci. Rev.* **2015**, *141*, 105−121.

(3) Blissett, R. S.; Rowson, N. A. A review of the multi-component utilization of coal fly ash. *Fuel* **2012**, *97*, 1−23.

(4) Ahmaruzzaman, M. A review of the utilization of fly ash. *Prog. Energy Combust. Sci.* **2010**, *36*, 327−363.

(5) Gollakota, A. R. K.; Volli, V.; Shu, C.-M. Progressive utilisation prospects of coal fly ash: A review. *Sci. Total Environ.* **2019**, *672*, 951−989.

(6) Ramme, B. W.; Tharaniyil, M. P. *Coal Combustion Products Utilization Handbook*, 3rd ed.; A We Energies Publication: Milwaukee, Wisconsin, 2013.
(7) Ahmaruzzaman, M.; Gupta, V. K. Application of coal fly ash in air quality management. *Ind. Eng. Chem. Res.* **2012**, *51*, 15299−15314.
(8) Wang, N.; Sun, X.; Zhao, Q.; Yang, Y.; Wang, P. Leachability and adverse effects of coal fly ash: A review. *J. Hazard. Mater.* **2020**, *396*, 122725.
(9) Wang, S. Application of Solid Ash Based Catalysts in Heterogeneous Catalysis. *Environ. Sci. Technol.* **2008**, *42*, 7055−7063.
(10) Ranjbar, N.; Kuenzel, C. Cenospheres: A review. *Fuel* **2017**, *207*, 1−12.
(11) Bartoňová, L. Unburned carbon from coal combustion ash: An overview. *Fuel Process. Technol.* **2015**, *134*, 136−158.
(12) Valeev, D.; Kunilova, I.; Alpatov, A.; Mikhailova, A.; Goldberg, M.; Kondratiev, A. Complex utilisation of ekibastuz brown coal fly ash: Iron & carbon separation and aluminum extraction. *J. Cleaner Prod.* **2019**, *218*, 192−201.
(13) Anshits, N. N.; Mikhailova, O. A.; Salanov, A. N.; Anshits, A. G. Chemical composition and structure of the shell of fly ash non-perforated cenospheres produced from the combustion of the Kuznetsk coal (Russia). *Fuel* **2010**, *89*, 1849−1862.
(14) Sharonova, O. M.; Anshits, N. N.; Solovyov, L. A.; Salanov, A. N.; Anshits, A. G. Relationship between composition and structure of globules in narrow fractions of ferrospheres. *Fuel* **2013**, *111*, 332−343.
(15) Fomenko, E. V.; Anshits, N. N.; Solovyov, L. A.; Mikhaylova, O. A.; Anshits, A. G. Composition and Morphology of Fly Ash Cenospheres Produced from the Combustion of Kuznetsk Coal. *Energy Fuels* **2013**, *27*, 5440−5448.
(16) Fomenko, E. V.; Anshits, N. N.; Vasilieva, N. G.; Mikhaylova, O. A.; Rogovenko, E. S.; Zhizhaev, A. M.; Anshits, A. G. Characterization of Fly Ash Cenospheres Produced from the Combustion of Ekibastuz Coal. *Energy Fuels* **2015**, *29*, 5390−5403.
(17) Sharonova, O. M.; Anshits, N. N.; Anshits, A. G. Composition and morphology of narrowly sized ferrospheres isolated from various types of fly ash. *Inorg. Mater.* **2013**, *49*, 586−594.
(18) Bayukov, O. A.; Anshits, N. N.; Balaev, A. D.; Sharonova, O. M.; Rabchevskii, E. V.; Petrov, M. I.; Anshits, A. G. Mossbauer study of magnetic microspheres isolated from power plant fly ash. *Inorg. Mater.* **2005**, *41*, 50−59.
(19) Bajukov, O. A.; Anshits, N. N.; Petrov, M. I.; Balaev, A. D.; Anshits, A. G. Composition of ferrospinel phase and magnetic properties of microspheres and cenospheres from fly ashes. *Mater. Chem. Phys.* **2009**, *114*, 495−503.
(20) Anshits, A. G.; Kondratenko, E. V.; Fomenko, E. V.; Kovalev, A. M.; Bajukov, O. A.; Anshits, N. N.; Sokol, E. V.; Kochubey, D. I.; Boronin, A. I.; Salanov, A. N.; Koshcheev, S. V. Physicochemical and catalytic properties of glass crystal catalysts for the oxidation of methane. *J. Mol. Catal. A: Chem.* **2000**, *158*, 209−214.
(21) Anshits, A. G.; Bayukov, O. A.; Kondratenko, E. V.; Anshits, N. N.; Pletnev, O. N.; Rabchevskii, E. V.; Solovyov, L. A. Catalytic properties and nature of active centers of ferrospheres in oxidative coupling of methane. *Appl. Catal., A* **2016**, *524*, 192−199.
(22) Kopytov, M. A.; Golovko, A. K.; Kirik, N. P.; Anshits, A. G. Thermal transformations of highmolecular-mass-components of heavy petroleum residues. *Pet. Chem.* **2013**, *53*, 14−19.
(23) Vereshchagina, T. A.; Fedorchak, M. A.; Sharonova, O. M.; Fomenko, E. V.; Shishkina, N. N.; Zhizhaev, A. M.; Kudryavtsev, A. N.; Frank, L. A.; Anshits, A. G. Ni^{2+}−zeolite/ferrosphere and Ni−silica/ferrospheres beads for magnetic affinity separation of histidinetagged proteins. *Dalton Trans.* **2016**, *45*, 1582−1592.
(24) Sarkar, A.; Rano, R.; Mishra, K. K.; Sinha, I. N. Particle size distribution profile of some Indian fly ash — a comparative study to assess their possible uses. *Fuel Process. Technol.* **2005**, *86*, 1221−1238.
(25) Moreno, N.; Querol, X.; Andrés, J.; Stanton, K.; Towler, M.; Nugteren, H.; Janssenjurkovicova, M.; Jones, R. Physico−chemical characteristics of European pulverized coal combustion fly ashes. *Fuel* **2005**, *84*, 1351−1363.
(26) Bhanarkar, A. D.; Gavane, A. G.; Tajne, D. S.; Tamhane, S. M.; Nema, P. Composition and size distribution of particules emissions from a coal−fired power plant in India. *Fuel* **2008**, *87*, 2095−2101.
(27) World Health Organization. *Ambient Air Pollution: A Global Assessment of Exposure and Burden of Disease*, 2016. https://www.who.int/phe/publications/air-pollution-global-assessment/en/.
(28) Lawson, M. J.; Prytherch, Z. C.; Jones, T. P.; Adams, R. A.; BéruBé, K. A. Iron-rich magnetic coal fly ash particles induce apoptosis in human bronchial cells. *Appl. Sci.* **2020**, *10*, 8368.
(29) Blaha, U.; Sapkota, B.; Appel, E.; Stanjek, H.; Rösler, W. Micro-scale grain-size analysis and magnetic properties of coal-fired power plant fly ash and its relevance for environmental magnetic pollution studies. *Atmos. Environ.* **2008**, *42*, 8359−8370.
(30) Kapper, K. L.; Bautista, F.; Goguitchaishvili, A.; Bógalo, M. F.; Cejudo-Ruíz, R.; Cervantes Solano, M. The use and misuse of magnetic methods to monitor environmental pollution in urban areas. *Bol. Soc. Geol. Mex.* **2020**, *72*, 1−44.
(31) Liu, Q.; Roberts, A. P.; Larrasoaña, J. C.; Banerjee, S. K.; Guyodo, Y.; Tauxe, L.; Oldfield, F. Environmental Magnetism: Principles and Applications. *Rev. Geophys.* **2012**, *50*, 1−50.
(32) Fomenko, E. V.; Anshits, N. N.; Kushnerova, O. A.; Akimochkina, G. V.; Kukhtetskiy, S. V.; Anshits, A. G. Separation of nonmagnetic fine narrow fractions of PM_{10} from coal fly ash and their characteristics and mineral precursors. *Energy Fuels* **2019**, *33*, 3584−3593.
(33) Reed, S. J. B. *Electron Microprobe Analysis and Scanning Electron Microscopy in Geology*, 2nd ed.; Cambridge University Press: New York, 2005.
(34) Sharonova, O. M.; Anshits, N. N.; Fedorchak, M. A.; Zhizhaev, A. M.; Anshits, A. G. Characterization of ferrospheres recovered from high-calcium fly ash. *Energy Fuels* **2015**, *29*, 5404−5414.
(35) Anshits, N. N.; Fedorchak, M. A.; Fomenko, E. V.; Mazurova, E. V.; Anshits, A. G. Composition, structure, and formation routes of blocklike ferrospheres separated from coal and lignite fly ashes. *Energy Fuels* **2020**, *34*, 3743−3754.
(36) Wu, J.; Tou, F.; Yang, Y.; Liu, C.; Hower, J. C.; Baalousha, M.; Wang, G.; Liu, M.; Hochella, M. F., Jr. Metal-containing nanoparticles in low-rank coal-derived fly ash from China: characterization and implications toward human lung toxicity. *Environ. Sci. Technol.* **2021**, *55*, 6644−6654.
(37) Zhang, Q.; Lu, D.; Wang, D.; Yang, X.; Zuo, P.; Yang, H.; Fu, Q.; Liu, Q.; Jiang, G. Separation and tracing of anthropogenic magnetite nanoparticles in the urban atmosphere. *Environ. Sci. Technol.* **2020**, *54*, 9274−9284.
(38) Sutto, T. E. Magnetite fine particle and nanoparticle environmental contamination from industrial uses of coal. *Environ. Pollut.* **2018**, *243*, 528−533.
(39) Li, Z.; Ji, Y.; Ma, H.; Zhao, P.; Zeng, X.; Liu, S.; Jiang, Y.; Wang, L.; Liu, A.; Gao, H.; Liu, F.; Mwangi, J. K. Characterization of inorganic elements within $PM_{2.5}$ and PM_{10} fractions of fly ashes from coal-fired power plants. *Aerosol Air Qual. Res.* **2017**, *17*, 1105−1116.
(40) Herzenberg, C. L.; Toms, D. Mössbauer absorption measurements in iron−containing minerals. *J. Geophys. Res.* **1966**, *71*, 2661−2677.
(41) Da Costa, G. M.; De Grave, E.; Vandenberghe, R. E. Mössbauer studies of magnetite and Al-substituted maghemites. *Hyperfine Interact.* **1998**, *117*, 207−243.
(42) Krupička, S. *Physik der Ferrite und der verwandten Magnetischen Oxide*. (Physics of Ferrites and Related Magnetic Oxides) (in German); Springer-Verlag, Friedr.Vieweg + Sohn: Braunschweig, 1973.
(43) Tronc, E.; Chanéac, C.; Jolivet, J. P. Structural and magnetic characterization of ε Fe2O3. *J. Solid State Chem.* **1998**, *139*, 93−104.
(44) Xu, H.; Lee, S.; Xu, H. Luogufengite: A new nano−mineral of Fe_2O_3 polymorph with giant coercive field. *Am. Mineral.* **2017**, *102*, 711−719.
(45) Yakushkin, S. S.; Balaev, D. A.; Dubrovskiy, A. A.; Semenov, S. V.; Knyazev, Y. V.; Bayukov, O. A.; Kirillov, V. L.; Ivantsov, R. D.; Edelman, I. S.; Martyanov, O. N. ε-Fe2O3 nanoparticles embedded in

https://doi.org/10.1021/acsomega.1c03187
ACS Omega 2021, 6, 20076−20085

silica xerogel−magnetic metamaterial. *Ceram. Int.* **2018**, *44*, 17852−17857.
(46) Sakurai, S.; Namai, A.; Hashimoto, K.; Ohkoshi, S.-i. First observation of phase transformation of all four Fe_2O_3 phases ($\gamma \rightarrow \varepsilon \rightarrow \beta \rightarrow \alpha$-phase). *J. Am. Chem. Soc.* **2009**, *131*, 18299−18303.
(47) Zhao, D.; Huo, Q.; Feng, J.; Chmelka, B. F.; Stucky, G. D. Nonionic triblock and star diblock copolymer and oligomeric surfactant syntheses of highly ordered, hydrothermally stable, mesoporous silica structures. *J. Am. Chem. Soc.* **1998**, *120*, 6024−6036. This notice is correction: J. Am. Chem. Soc. 2014, 136 (29), 10546; DOI 10.1021/ja506344k
(48) Bukhtiyarova, G. A.; Mart'yanov, O. N.; Yakushkin, S. S.; Shuvaeva, M. A.; Bayukov, O. A. State of iron in nanoparticles prepared by impregnation of silica gel and aluminum oxide with $FeSO_4$ solutions. *Phys. Solid State* **2010**, *52*, 826−837.
(49) Mack, D. E.; Becker, K. D.; Schneider, H. High-temperature Mossbauer study of Fe-substituted mullite. *Am. Mineral.* **2005**, *90*, 1078−1083.
(50) Dubrovskiy, A. A.; Balaev, D. A.; Shaykhutdinov, K. A.; Bayukov, O. A.; Pletnev, O. N.; Yakushkin, S. S.; Bukhtiyarova, G. A.; Martyanov, O. N. Size effects in the magnetic properties of ε-Fe_2O_3 nanoparticles. *J. Appl. Phys.* **2015**, *118*, 213901.
(51) Johnson, H. P.; Lowrie, W.; Kent, D. V. Stability of anhysteretic remanent magnetization in fine and coarse magnetite and maghemite particles. *Geophys. J. Int.* **1975**, *41*, 1−10.
(52) Smirnov, A. V. Grain size dependence of low-temperature remanent magnetization in natural and synthetic magnetite: Experimental study. *Earth, Planets Space* **2009**, *61*, 119−124.
(53) Banerjee, S. K.; Moskowitz, B. M. Ferrimagnetic properties of magnetite. In *Magnetite Biomineralization and Magnetoreception in Organisms*; Kirschvink, J. L., Jones, D. S., MacFadden, B. J., Eds.; Topics in Geobiology, V. 5; Springer: Boston, MA, 1985; p 17.
(54) Sung Lee, J.; Myung Cha, J.; Young Yoon, H.; Lee, J.-K.; Keun Kim, Y. Magnetic multi-granule nanoclusters: A model system that exhibits universal size effect of magnetic coercivity. *Sci. Rep.* **2015**, *5*, 12135.
(55) Dunlop, D. J. The rock magnetism of fine particles. *Phys. Earth Planet. Inter.* **1981**, *26*, 1−26.
(56) Pauthenet, R. Variation thermique de l'aimantation spontanee des ferrites de nickel, cobalt, fer et manganese. *C. R. Acad. Sci., Sér. B* **1950**, *230*, 1842−1844.
(57) Stoner, E. L.; Wohlfarth, E. P. A mechanism of magnetic hysteresis in heterogeneous alloys. *Philos. Trans. R. Soc., A* **1948**, *240*, 599−642.
(58) Semenov, S. V.; Balaev, D. A.; Balaev, D. A.; Shaykhutdinov, K. A.; Rogozin, D. Y. Day Plots of Bacterial Magnetite from Sediments of Shira Lake (Khakassia, Russia). *J. Sib. Fed. Univ., Chem.* **2017**, *10*, 252−256.
(59) Knyazev, Y. V.; Tarasov, A. S.; Platunov, M. S.; Trigub, A. L.; Bayukov, O. A.; Boronin, A. I.; Solovyov, L. A.; Rabchevskii, E. V.; Shishkina, N. N.; Anshits, A. G. Structural and electron transport properties of $CaFe_2O_4$ synthesized in air and in helium atmosphere. *J. Alloys Compd.* **2020**, *820*, 153073.

https://doi.org/10.1021/acsomega.1c03187
ACS Omega 2021, 6, 20076−20085